

# Characterising Instrumentation Canister Aerodynamics on the FAAM BAe-146-301 Atmospheric Research Aircraft

C J Bennett<sup>1</sup>, G J Nott<sup>2</sup>, A Wellpott<sup>3</sup>, N Lawson<sup>4</sup>, M Delise<sup>5</sup>, B Woodcock<sup>6</sup>, and G B Gratton<sup>7</sup>

<sup>1</sup>National Flying Laboratory Centre, School of Aerospace, Transport and Manufacturing,  
Cranfield University, UK., Email: C.J.Bennett@Cranfield.ac.uk

<sup>2</sup>Facility for Airborne Atmospheric Measurements (FAAM), Bedfordshire, UK

<sup>3</sup>Facility for Airborne Atmospheric Measurements (FAAM), Bedfordshire, UK

<sup>4</sup>National Flying Laboratory Centre, School of Aerospace, Transport and Manufacturing,  
Cranfield University, UK.

<sup>5</sup>National Flying Laboratory Centre, School of Aerospace, Transport and Manufacturing,  
Cranfield University, UK.

<sup>6</sup>Aventech Research Inc, Ontario, Canada

<sup>7</sup>Facility for Airborne Atmospheric Measurements (FAAM), Bedfordshire, UK

## ABSTRACT

A Computational Fluid Dynamic (CFD) investigation is aimed at accurately predicting the air flow characteristics in the vicinity of under-wing mounted instruments on the Facility for Airborne Atmospheric Measurement's (FAAM) BAe-146-301. Perturbation of the free stream airflow as it passes through the region of detection of the under-wing instruments, may lead to additional uncertainties in the measurement of clouds and cloud particles. The CFD model was validated with flight data from an Aircraft-Integrated Meteorological Measurement System (AIMMS-20) in a wing-mounted instrument canister. Flow predictions show a consistent slowing from the true air speed of the aircraft in the longitudinal direction and horizontal and vertical flows up to 10% of the air speed being introduced. The potential impact of these flow perturbations on sizing of particles

24 with Cloud Imaging Probes is modelled. Sizing errors are dependent on the methodology used and  
25 the shape of the particle, those due to transverse flows remain very small but miss-sizing due to  
26 unaccounted longitudinal flow perturbations are potentially more serious.

## 27 **Acknowledgements**

28 Airborne data was obtained using the BAe-146-301 Atmospheric Research Aircraft flown by  
29 Airtask Ltd and managed by the Facility for Airborne Atmospheric Measurements (FAAM), which  
30 is a joint entity of the Natural Environment Research Council (NERC) and the UK Met Office.

## 31 **INTRODUCTION**

32 The Facility for Airborne Atmospheric Measurements (FAAM) is a publicly funded research  
33 facility that, as part of the National Centre for Atmospheric Science (NCAS), supports atmospheric  
34 research in the United Kingdom by providing an instrumented large atmospheric research aircraft  
35 (ARA) and associated services. The ARA is a BAe-146-301 aircraft, registration G-LUXE, owned  
36 by the National Environment Research Council and flown by Airtask Group Ltd. The aircraft has  
37 been extensively modified to carry 19” rack-based instruments within the cabin, canister-based  
38 instruments affixed to underwing pylons, and remote sensing instruments carried on the roof, belly,  
39 and inside a blister affixed to the port side of the fore section of the fuselage. The exact instrument  
40 fit changes based on the scientific objectives of each flight. The aircraft carries 3 crew and up to 18  
41 scientists who operate the research equipment.

42 This study focuses on the instrument cluster mounted on the underside of the port wing, see Fig.  
43 1 which shows four different probes fitted in the four canister positions. In the upper-outer position  
44 is the Cloud Imaging Probe (CIP100), in the upper-inner position is the Passive Cavity Aerosol  
45 Spectrometer Probe (PCASP), the lower-inner canister houses the Cloud Droplet Probe (CDP)  
46 all manufactured by Droplet Measurement Technologies Inc, and in the lower-outer position is  
47 the Aircraft-Integrated Meteorological Measurement System (AIMMS-20) by Aventech Research  
48 Inc. The PCASP, CDP, and CIP100 measure aerosol and cloud particles over nominal size ranges  
49 of 0.1–3 $\mu\text{m}$ , 3–50 $\mu\text{m}$ , and 100-6200 $\mu\text{m}$  respectively. The AIMMS samples meteorological data

50 (temperature, humidity and pressure data), aircraft attitude data, and 3-dimensional winds with a  
51 5-port probe positioned on a 0.425m boom.

52 The aim of this paper is to investigate the air flow characteristics within the measurement zone  
53 of the open-path instruments, for example the CIP100 and CDP as shown in Fig. 1. Due to the  
54 inertia of larger hydrometeors such as cloud and precipitation particles, these particles must be  
55 measured by open-path instruments mounted on booms or pylons rather than with cabin-based  
56 instruments which require inlets on the aircraft's skin Wilson and Jonsson (2011). The open-path  
57 instruments discussed in this work are laser based imaging probes which record particle shadows  
58 on a one-dimensional detector array as they pass through the sample volume. A broad range of  
59 particle sizes from tens of micrometres to several centimetres may be measured by this type of  
60 instrument.

61 There are a number of factors which can affect the air flow characteristics within the measure-  
62 ment zone of open-path instruments. The redirection/deflection of air flow around the airframe  
63 (including the instrument cluster itself), congestion/compression of the airflow immediately up-  
64 stream of the instrument Weigel et al. (2016); Korolev et al. (2012), pressure gradients generated  
65 by lifting surfaces such as the wings, and pressure gradients generated by the engines may all affect  
66 the air flow direction/angle, speed, and quality (laminar/turbulent) in the instrument's measurement  
67 zone.

68 Firstly, if the flow direction through the sample volume is altered, imaged particles may appear  
69 uniformly skewed at an angle. MacPherson and Baumgardner MacPherson and Baumgardner  
70 (1988) demonstrate this in a study of a Beechcraft King Air. It is shown that a transverse flow  
71 skews particles proportionally to the ratio of transverse to longitudinal flow speeds. This effect is  
72 dependent on particle inertia, related to the size of each particle Twohy and Rogers (1993), and  
73 hence will skew the measured particle size distribution.

74 Secondly, the speed of air through the instrument sample volume or probe air speed (PAS) is  
75 important as it is used, when combined with the two dimensional sample area as defined by the laser  
76 geometry, to convert an internal clock time step into a volumetric flow rate. Then, with the number

77 of particles in a given time interval counted, a volumetric number concentration of particles can  
78 be calculated. Hence, if the PAS diverges from the aircraft true air speed (TAS), and this is not  
79 accounted for, the measured number concentration may be affected Korolev et al. (2012).

80 Finally, convergence and divergence of flow lines may also change the concentration of particles  
81 passing through the probe's sample volume relative to the ambient concentration Twohy and Rogers  
82 (1993). Again, this effect is dependent on the inertia for a range of particle sizes.

83 Therefore, understanding the air flow characteristics at different flight conditions may allow the  
84 deviations in measured particle population, compared to the unperturbed ambient, to be compen-  
85 sated for. At the very least, the impact on the uncertainty of the measurements will be revealed.  
86 Clearly, these features are highly aircraft/instrument specific, but are analysed here for a BAe-146  
87 as an example of the methodology which can be employed to better understand the performance  
88 and correlation of instruments used in atmospheric research.

89 Flow modelling for the aircraft was done during the initial conversion of the aircraft for its current  
90 atmospheric research role using a very simplified shape representation and standard Engineering  
91 Sciences Data Unit (ESDU) data sheets. However, these have not the required precision, particularly  
92 around the wing pylons, to quantify the effects of flows on particle measurements. In 2015 the  
93 aircraft was laser scanned to provide the basis for a Computational Fluid Dynamics (CFD) model  
94 of the aircraft. Flow data from the AIMMS shall be used to validate the model around the pylons.  
95 Normally, the AIMMS data is calibrated for a particular position on the aircraft by performing a  
96 series of prescribed manoeuvres that are designed to account for the position of the probe relative  
97 to the centre of the aircraft, for computing the attitude solution, and for any flow perturbations due  
98 to the aircraft. However, for this study, the AIMMS wind data was processed without the second set  
99 of calibration coefficients applied to obtain the raw air flow vector. The AIMMS data thus provides  
100 actual angle of attack (AOA) and sideslip (AOSS) as measured at the location of the probe.

## 101 **CFD METHODOLOGY**

102 A full-scale solid model of the aircraft was produced from a point cloud obtained from a  
103 Leica ScanStation P20. Multiple scans of the aircraft were performed from different angles,

104 above and below the fuselage, while the aircraft was positioned in the hanger, yielding a complete  
105 and comprehensive point cloud. The expected accuracy of the scan was  $\pm 3\text{mm}$  as specified in  
106 the manufacturer data sheet. Following the scan, the data was transferred to Leica Geosystems  
107 Cyclone software which, with a 2mm constraint, allowed registration and unification of the multiple  
108 point clouds into a single dataset. The file was finally output as an STL file for inputting into the  
109 Computer Aided Design (CAD) package CATIA.

110 CATIA was used to produce a series of surfaces defined through curves generated from the  
111 point cloud. Where possible, multiple surfaces were concatenated to minimise the total number of  
112 surfaces used to describe the aircraft. Finally, the CATIA solid model was outputted as an IGES  
113 file for importing into the meshing software ANSYS ICEM CFD. Table 1 summarises the key  
114 dimensions of the aircraft.

115 ANSYS ICEM CFD was used to generate an unstructured mesh via the octree method, consisting  
116 of tri surface elements and tetra volume cells. Smoothing was subsequently applied to increase  
117 the overall mesh quality. Several mesh densities were produced in order to refine the model, the  
118 coarsest of which had 6 million cells and the finest 15 million. The cylindrical domain was specified  
119 with 10 times the characteristic length of the aircraft downstream, 5 times the characteristic length  
120 upstream, and 5 times the characteristic length for the radius. A mesh refinement study Delise  
121 (2017) revealed that a mesh with fine detail on and around the pylons and canisters, but relatively  
122 low density elsewhere (12.5 million cells in total) provided adequate accuracy in terms of lift and  
123 drag coefficients, as well as flow angles and velocities upstream of the canisters, compared to finer  
124 density meshes. The model was created without probes installed in the canisters. The ends of the  
125 canisters have been blanked with hemispherical domes and these are included in the model.

126 As is conventional for high speed compressible flows MacCormack (1981), solutions were  
127 sought via an implicit, steady state, density based solver in ANSYS Fluent v16 for all cases.  
128 Simulation parameters were specified to represent cruise conditions for which reliable flight-test  
129 data had previously been acquired, see Table 2.

130 Adequate convergence of the solutions was considered when RMS perturbations of the lift and

131 drag coefficients were less than  $1 \times 10^{-4}$ , Roache (1998). This was achieved by initially specifying  
132 a first order solution, and then gradually blending in the second order terms until a full second order  
133 solution had converged, and was typically achieved in approximately 35,000 iterations.

134 Prior to conducting the full matrix of CFD simulations using the developed model, two test cases  
135 were analysed to understand if the model could be simplified while still maintaining representative  
136 flow angles in the vicinity of the probe measurement location. A plot line is defined, see Fig. 2,  
137 to analyse the air flow upstream of the AIMMS. The line is coaxial with the boom on which the  
138 probe is installed, but extends further into the upstream airflow approximately 12m. The flow angle  
139 analysis followed the same methodology as in a previous publication regarding the response of angle  
140 of attack and sideslip angle vanes fitted to the nose of a Jetstream 31 Bennett et al. (2017a,b). The  
141 following two subsections discuss the effect on the air flow angles when the engine is in operation,  
142 and also the use of of viscous/inviscid solvers.

### 143 **Engine Operative and Inoperative Comparison**

144 Analysis was undertaken to quantify the effect of the turbofan engines on the flow characteristics  
145 in the vicinity of the AIMMS probe. The CFD model incorporates two disks at the inlet and outlet  
146 of the engines. Isentropic flow theory Massey and Ward-Shith (1998) was used to estimate the  
147 pressure jump through the nozzle, assuming that in cruise conditions ( $M \approx 0.5$ ) the engine inlet is at  
148 95% atmospheric pressure with inlet velocity of  $M \approx 0.2$ , and at the outlet the flow is accelerated to  
149  $M \approx 0.9$  to give a pressure recovery of 96% of the atmospheric value. Based on typical combustion  
150 temperatures and pressures for the Lycoming ALF-507-1H turbofan engine used on this aircraft,  
151 and the physical dimensions obtained from scale drawings, the pressure at the outlet was calculated  
152 to be approximately 60,000Pa and the temperature 345K. The inlet and outlet conditions were  
153 defined as pressure inlet and outlet boundary conditions in the Fluent case files.

154 Fig. 3 shows a comparison of the air flow angles, along the plot line shown in Fig. 2, for the  
155 engine in operation and inoperative at  $5^\circ$  AOA and  $0^\circ$  AOSS; note that compared to typical airliner  
156 operation, this is a relatively high AOA because the FAAM aircraft typically operates close to best  
157 endurance speed (termed 'Science Speed') rather than slightly above best range speed. It is seen that

158 at  $x = 0$  the air flow approaches the free stream conditions (AOA (x-z plane) $=5^\circ$ , AOSS (x-y plane)  
159  $=0^\circ$ ). As  $x$  increases, the upwash associated with the wing's leading edge gradually intensifies  
160 (positive flow in the x-z plane) with an associated outboard flow (negative flow in the x-y plane)  
161 due to the swept and tapered nature of the wing. From  $x \approx 0.7$ , the flow angle changes radically  
162 as other parts of the aircraft exert an influence on the airflow. There is a turning point at  $x \approx 0.73$   
163 due to the geometry of the engine cowling/casing which causes the upwards and outboard flows to  
164 weaken in magnitude. The vertical and horizontal flow angles then further increase dramatically at  
165  $x \approx 0.95$  and  $x \approx 0.85$  respectively to the stagnation point at the canister dome. It is seen that at the  
166 AIMMS measurement location, for this particular case, the vertical flow angle has been reduced  
167 and the horizontal flow forced outboard compared to the free stream condition.

168 Comparing the solid and dotted lines in Fig. 3, it is seen that that the engine's operation has  
169 minimal effect on the flow angle in the x-z (vertical) plane, but causes a reduction in flow angle  
170 in the x-y (transverse) plane in the vicinity of the AIMMS probe pressure ports of approximately  
171  $1.5^\circ$ . Hence, it was concluded that the engine's operation should be included in the full matrix of  
172 CFD simulations going forwards.

### 173 **Viscous and Inviscid Solver Comparison**

174 For the flight envelope considered in this paper, as seen in Table 2, the Reynolds numbers are  
175 of magnitude  $10^7$ . At high Reynolds number conditions such as these, the turbulent boundary  
176 layer on the probe is calculated to grow up to approximately 8mm (using  $\delta \approx 0.37x/\text{Re}_x^{1/5}$  where  
177  $x = 0.425\text{m}$  is the length of the probe, Re is calculated based on the conditions given in Table  
178 2, and a zero pressure gradient is assumed due to the constant diameter of the probe boom) and  
179 hence would not affect the airflow at the other three instrument positions as there is a minimum  
180 horizontal/vertical separation of 0.56m. Furthermore, due to the length of the probe boom, the  
181 measurement location is well upstream of any congestion effects caused by the stagnation point on  
182 the canister dome, as discussed by Korolev in Korolev et al. (2012).

183 Fig. 4 shows a comparison of the flow angles, along the plot line in Fig. 2, for inviscid and  
184 viscous solutions at  $5^\circ$  AOA and  $0^\circ$  AOSS. The plots, in general, exhibit the same characteristics

185 as in Fig. 3. Comparing the solid and dashed lines, it is seen that the results are well matched,  
186 differing by a maximum of  $0.1^\circ$  across the observed range. Therefore, it is concluded that the use of  
187 an unstructured mesh with inviscid solver provides sufficiently accurate and representative results  
188 compared to a fully structured mesh with prism layers treated with the Spalart-Allmaras turbulence  
189 model. This allowed significant computational expense can be spared by reducing the size of the  
190 mesh due to the omission of the prism layers, and using an inviscid solver in Fluent.

### 191 **Anti-Icing Vents**

192 It is worth noting that the aircraft has anti-icing vents on the underside of the wings. This is  
193 essentially a bleed air system which routes hot air from the engines to outlets on the lower surface  
194 of the wings. Although the air is exhausted upstream of the probe location at approximately  $200^\circ\text{C}$ ,  
195 it is assumed that the flow rate is not high enough to affect the airflow onto the probe, which is  
196 positioned approximately 1m below the wing.

### 197 **Final Model and Identification of Comparable Flight Test data**

198 In the subsections above, justification for inclusion of the engine effects, but using an unstruc-  
199 tured mesh with inviscid solver, is confirmed. It was assumed, therefore, that the main factors  
200 affecting the airflow direction and velocity at the AIMMS probe measuring location are the engine  
201 effects, redirection/deflection of airflow around the airframe, and the pressure field generated by  
202 the wing.

203 To investigate fully, a matrix of CFD simulations were specified with appropriate conditions to  
204 collate the final set of results with which to compare to flight test data. AIMMS data from flight  
205 B875 was used for the validation of the final CFD model. This flight took place on 28 November  
206 2014 off the north west coast of Scotland. Three suitable straight and level runs were identified  
207 with average altitudes of 88m ( $\sim 300\text{ft}$ ), 7,610m ( $\sim 25,000\text{ft}$ ), and 10,271m ( $\sim 33,700\text{ft}$ ) with the  
208 CFD model validation work been done using static conditions for 7,610m ( $\sim 25,000\text{ft}$ ). At this  
209 altitude, 4 hrs and 10 mins into the flight, and with these flight conditions the relationship between  
210 AOA as measured by the radome 5-port turbulence probe and TAS was found and shown in Table  
211 2.



212 The x-axis reference for the CFD model is parallel to the aircraft seat rail datum, this reference  
213 is also used by the on-board GPS-aided Inertial Navigation system which records aircraft pitch  
214 during flight. Comparisons of the model and AIMMS data is presented in terms of AOA and to  
215 ensure that the aircraft AOA was the same as the model AOA, the pitch was plotted against AOA  
216 as measured with the nose-mounted turbulence probe (assumed to be free of flow distortions). The  
217 slope of the fit was found to be 1.02 with an  $r^2$  value of 0.93 for the 7,610m (~ 25,000ft) flight  
218 leg. Therefore, the modelled AOA at the AIMMS location and the AOA measured by the AIMMS  
219 probe, are comparable.

## 220 RESULTS

221 The CFD results are compared to the in-flight AIMMS data for comparable conditions in Fig.  
222 5. The x-axis displays the ‘true’ AOA, and the y-axis displays the ‘measured’ AOA at the AIMMS  
223 probe, for each set of data. For the case of the CFD data, the ‘true’ AOA is given by the simulation  
224 set-up flow angle. For the case of the flight test data, the ‘true’ AOA is provided by the 5-hole probe  
225 located in the radome. It is also worth stating that the flight test data has been shifted by  $3.1^\circ$  to  
226 match the fuselage reference line used in the CFD simulations since the AIMMS canister has been  
227 mounted on the aircraft  $3.1^\circ$  nose-down relative to the aircraft datum. Furthermore, the flight test  
228 data has been filtered to contain only data points with  $\pm 0.2^\circ$  AOSS. The linear fit of the flight data  
229 has a slope of 1.32 compared to 1.56 for the model, with  $r^2=0.95$ . Also, 95% confidence intervals  
230 have been added to each set of data. The confidence interval for the CFD results also includes a  
231 potential error due to the  $\pm 3$ mm accuracy of the laser scan used to generate the aircraft model.

232 Both sets of data show that the air flow angle in the vicinity of the AIMMS probe is decreased  
233 as compared to the freestream value. As discussed above, this effect is understood to be due to the  
234 engines, redirection/deflection of the airflow around the aircraft, and the pressure field generated  
235 below the wing with associated upwash. Fig. 6 shows two different cut plane pressure contours  
236 (x-z upper and x-y lower) to illustrate this. The measurement location of the AIMMS probe clearly  
237 lies within a region of high pressure caused by a combination of effects: the port outer engine’s  
238 operation, the wing generating lift, the redirection/deflection of air flow around the engine casing.

239 It is seen from Fig. 5 that the CFD results provide good consistency, with confidence intervals  
240 of approximately  $\pm 0.1^\circ$ . The filtered flight test data also exhibits minimal scatter, giving confidence  
241 intervals of approximately  $\pm 0.2^\circ$ . This was the primary reason for selecting the data set at 7,610m  
242 ( $\sim 25,000$ ft); The data was evidently much less susceptible to scatter due to turbulence, for example.  
243 The uncertainty of individual AOA measurements of the AIMMS has not been included in the  
244 calculation of the confidence intervals.

245 The CFD model performs well despite, in general, over predicting the AIMMS probe flow angle  
246 within the flight test range up to a maximum of  $0.28^\circ$ . The CFD prediction is most accurate at  
247 the lower end of the flight test range, around  $4.6^\circ$  angle of attack, where the two lines of best fit  
248 intersect. However, since the CFD and flight test data trend lines have a gradients of 1.56 and 1.32  
249 respectively, the prediction diverges at the higher angle of attack range. Despite this, for a typical  
250 flight condition, for example 7,610m ( $\sim 25,000$ ft),  $5^\circ$  AOA, and  $0^\circ$  AOSS, the CFD model over  
251 predicts the flow angle at the AIMMS probe by just  $0.09^\circ$ . The discrepancy in the results may in  
252 part be due to inaccuracy of the 5-hole probe in the radome, which is assumed here to provide a  
253 'true' AOA for the flight test data. Without the benefit of a boom style AOA sensor, or specific data  
254 regarding the accuracy of the 5-hole probe, the results must rely on this assumption.

255 The flow velocity perturbations for all four of the canister positions were found using the CFD  
256 model for a range of AOA at 7,610m ( $\sim 25,000$ ft). Fig. 7(a) plots the longitudinal velocity scaling  
257 relative to TAS and shows a slowing of the free-stream velocity for all positions, the magnitude  
258 of which increases with AOA. The canisters experience a decrease of 3-12% in longitudinal flow  
259 velocity across the operating conditions. The transverse velocity perturbations have opposite signs  
260 for canisters on either side of the pylon. Inboard canisters experience a flow towards the fuselage,  
261 positive values in Fig. 7(b), due to the influence of the engine cowling, while there is a flow towards  
262 the wing tip at the outboard canisters. The free-stream horizontal component is zero (AOSS= 0)  
263 while the perturbed flows vary by approximately 12% of TAS, that is  $\pm 6$ m/s transverse flows for a  
264 TAS of 100m/s, or  $\pm 19$ m/s at 150m/s. The vertical flow perturbation (not shown) is always negative,  
265 due to the influence of the wing, with the upper canister positions experiencing perturbations of

266 9-10% of TAS compared to 5-7% for the lower positions. The cowling and nacelle also exert an  
267 influence in the x-z plane, vertical flows at the inner canister positions having approximately 1%  
268 less downward perturbation than at the outer positions. It should be noted that the flow disturbances  
269 here are due only to the influence of the aircraft, the effect of the probes themselves is not included.  
270 The design of the probes has been shown to have a significant compressive effect on the flow  
271 through the sample volume but this depends on the design of the individual probes Weigel et al.  
272 (2016). Inclusion of this effect is beyond the scope of the presented work however the perturbations  
273 due to the probe itself may be comparable to those caused by the airframe for several common  
274 probe types, that is approximately 5% Korolev et al. (2012). Weigel et al. Weigel et al. (2016)  
275 present measured perturbations of greater than 20% which include the effect of both the aircraft,  
276 in their case a Gulfstream G-550, and the probes. The canister position relative to the wing and  
277 engine cowling means that probes in different positions will experience different flows. Particles  
278 of different sizes shall be affected by the different flow vectors and the implementation of particle  
279 flow into the CFD model is a subject of ongoing work.

## 280 **IMPACT OF AIR FLOW ON OPTICAL ARRAY PROBES**

281 Optical array probes were developed Knollenberg (1970) to determine the particle size distribu-  
282 tion and shape of cloud and precipitation particles. Particles pass through an expanded laser beam  
283 and the shadow cast is measured on a one dimensional array. The array is read on a nanosecond  
284 time scale with the detector clock frequency and the particle/air speed through the laser beam de-  
285 termining the longitudinal resolution of the probe. The transverse resolution is determined by the  
286 pixel size and magnification of the imaging optics and may range from  $10\mu\text{m}$  to  $150\mu\text{m}$  depending  
287 on the probe.

288 A simple model has been made that digitises an arbitrarily-shaped particle with a 64 pixel linear  
289 array, the array size used in the Droplet Measurement Technologies Cloud Imaging Probe (CIP)  
290 as flown on the aircraft. The model particle can be stretched and skewed to simulate a particle  
291 carried through the probe sample volume with a perturbed airspeed and direction. Fig. 8 shows a  
292 spherical water droplet and the image produced by a  $15\mu\text{m}$  resolution CIP for both the unperturbed

293 airflow case and the case when there is a -20% change in the longitudinal and a 10% change in  
294 the transverse airflows. The degree of perturbation may be larger than realistic but has been used  
295 for visual clarity in both Figs. 8 and 9. The circle is both stretched, due to the particle passing  
296 through the sample volume more slowly, and skewed, due to the particle passing through the sample  
297 volume at an angle. The standard operating orientation of the CIPs on the aircraft is with the arms  
298 vertical. The transverse flow perturbations of interest in this case are thus horizontal. With the  
299 arms horizontal, the vertical airflow perturbations would be relevant.

300 The two dimensional image measured by the CIP is used to classify the three dimensional  
301 size and shape of the particle and there are a number of common methods for allocating a size  
302 to a particle of arbitrary shape Korolev and Isaac (2003); Wu and McFarquhar (2016). Fig. 9  
303 shows a synthetic hexagonal plate undergoing the same flow perturbations and sampling as for  
304 Fig. 8 and superimposed on the image are some common particle size definitions. The maximum  
305 transverse length, which is the maximum length in the plane of the photodiode array and shown  
306 as  $D_P$ , maximum longitudinal length, or length in the time dimension and shown as  $D_T$ , the  
307 hypotenuse of these two lengths,  $D_H$ , maximum length in any orientation,  $D_{\max}$ , and the length  
308 in the direction orthogonal to  $D_{\max}$ ,  $D_w$ , are common linear measurements. The diameter of the  
309 minimum enclosing circle,  $D_S$ , and the diameter of the area-equivalent circle,  $D_A$ , are also common  
310 and all are used to determine cloud and precipitation particle size distributions. The form of the  
311 reported size distribution shall be dependent on the definition used but importantly, may also be  
312 shifted due to any aforementioned image stretch and/or skew that has not been accounted for in the  
313 post-processing.

314 In order to illustrate the effect of stretch and skew, Fig. 10 shows the size scaling factor; that is  
315 the ratio of reported size for a perturbed particle image to that of the unperturbed particle image,  
316 of a spherical droplet as a function of longitudinal stretch and transverse skew. The scaling factor  
317 was found by performing a Monte-Carlo simulation with randomized size scaling and rotation  
318 of the same synthetic particle image. The results shown are for a droplet as this is the simplest  
319 case, however the same process was applied to a square, hexagonal plate (Fig. 9), a six-sided star

320 (approximating a dendrite), a rectangle (with aspect ratio 15:1 to approximate an ice needle), and  
321 an ice aggregate based on a real particle image presented in Wu and McFarquhar (2016). For  
322 the longitudinal perturbation shown in Fig. 10(a), the transverse size,  $D_P$ , is unchanged however  
323 the longitudinal dimension,  $D_T$ , and the area equivalent diameter are. A similar, approximately  
324 1:1 linear trend is seen when changing the clock frequency of a CIP in the laboratory as metallic  
325 circular dots are passed through the sample volume at constant speed. This is presented in terms  
326 of aspect ratio,  $D_T/D_P$ , by Weigel et al. Weigel et al. (2016) and is the inverse of a constant clock  
327 frequency while the air/particle speed through the instrument changes. Fig. 10(b) shows the impact  
328 of a transverse perturbation on the same size parameters. Here, the fractional change in size is  
329 significantly smaller and so the effect of digitization makes the data noisy. This is fortunate as this  
330 perturbation is significantly more difficult to account for. Some instruments include a pitot tube  
331 for local measurement of the PAS, this however does not measure transverse flow components.  
332 With randomized orientation, the average behaviour of shapes with an aspect ratio close to unity  
333 approaches that of a circle as the number of samples in the Monte-Carlo simulation increases. For  
334 the needle and aggregate however, a transverse perturbation results in a reduction in the apparent  
335 size of the particles of up to 2% for a 10% transverse velocity change. Thus the shape of the particle  
336 being measured by the probe shall effect the magnitude of any mis-sizing depending on the sizing  
337 metric being used.

## 338 CONCLUSIONS

339 CFD techniques have been used to predict the air flow characteristics in the vicinity of instru-  
340 ments fitted to underwing pylons on the FAAM BAe-146 atmospheric research aircraft (ARA).  
341 Data from the AIMMS at 7,610m (~25,000ft) during flight B875 was used to validate the model for  
342 a range of air speeds and AOA and show good agreement to within  $0.25^\circ$  on average and a gradient  
343 difference within 15%. Having validated the CFD model, the results were used to determine the  
344 flow perturbations due to the aircraft at all of the pylon instrument positions. Each of the positions  
345 experience different perturbations which also vary with aircraft AOA. Longitudinal flows slowed  
346 by a maximum of 12% while a transverse flow of up to  $\pm 6\%$  of TAS was introduced, with the sign

347 switching between inboard and outboard positions.

348 Influence of perturbation of the flows on cloud particle measurements was examined with  
349 a simple imaging probe simulation. Uncorrected changes in the longitudinal flow velocity can  
350 introduce particle size scaling, in the worst case relative changes in measured size may be as  
351 large as the relative change in velocity depending on the sizing metric used. The influence of  
352 the transverse perturbation is significantly less with size scaling of only up to 0.5% for realistic  
353 flight conditions. This is significantly less than other measurement uncertainties of the technique.  
354 Obtaining the flow perturbations from a CFD model at the measurement locations will improve  
355 accuracy of particle size measurements or at least improve understanding of sizing uncertainties.

356 Future enhancements to the study shall introduce particles into the flow model with the inclusion  
357 of accurate probe geometries (rather than modelling the canisters with a domed blank), and utilise  
358 a viscous model. To enable the analysis of the near-field effects in more detail. Additionally, a  
359 sensitivity study of the model is recommended to analyse the effect of altitude, airspeed, AOA,  
360 and AOSS on the flow perturbations introduced, so that the flows, and their effect on under-wing  
361 particle measurements, can be calculated for a broad range of applicable flight conditions.

## REFERENCES

- Bennett, C. J., Lawson, N. J., Gautrey, J., and Cooke, A. (2017a). “CFD simulation of flow around angle of attack and sideslip angle vanes on a BAe Jetstream 3102 - part 1.” *Aerospace Science and Technology*, 68, 561–576.
- Bennett, C. J., Lawson, N. J., Gautrey, J., and Cooke, A. (2017b). “CFD simulation of flow around angle of attack and sideslip angle vanes on a BAe Jetstream 3102 - part 2.” *Aerospace Science and Technology*, 68, 577–587.
- Delise, M. (2017). “Investigation of the turbofan jet effect upon the measurement canisters of the FAAM BAe 146-301.” M.S. thesis, Cranfield University, UK.
- Knollenberg, R. G. (1970). “The optical array: An alternative to scattering or extinction for airborne particle size determination.” *Journal of Applied Meteorology*, 9, 86–103.
- Korolev, A., Emery, E., and Creelman, K. (2012). “Modification and tests of particle probe tips to mitigate effects of ice shattering.” *Journal of Atmospheric and Oceanic Technology*, 30(4), 690–708.
- Korolev, A. and Isaac, G. (2003). “Roundness and aspect ratio of particles in ice clouds.” *Journal of Atmospheric Sciences*, 60(15), 1795–1808.
- MacCormack, R. W. (1981). “A numerical method for solving the equations of compressible viscous flows.” *AIAA*, 20(9), 1275–1281.
- MacPherson, J. and Baumgardner, D. (1988). “Airflow about King Air wingtip-mounted cloud particle measurement probes.” *Journal of Atmospheric and Oceanic Technology*, 5, 259–273.
- Massey, B. and Ward-Shith, J. (1998). *Mechanics of Fluids - Seventh Ed.* Nelson Thornes Ltd., UK.
- Roache, P. J. (1998). *Verification and Validation in Computational Science and Engineering.* Hermosa, New Mexico, USA.

386 Twohy, C. and Rogers, D. (1993). “Airflow and water-drop trajectories at instrument sampling  
387 points around the Beechcraft King Air and Lockheed Electra.” *Journal of Atmospheric and*  
388 *Oceanic Technology*, 10, 566–578.

389 Weigel, R., Spichtinger, P., Mahnke, C., Klingebiel, M., Afchine, A., Petzold, A., Kramer, M.,  
390 Costa, A., Molleker, S., Reutter, P., Szakall, M., Port, M., Grulich, L., Jurkat, T., Minikin, A.,  
391 and Borrmann, S. (2016). “Thermodynamic correction of particle concentrations measured by  
392 underwing probes on fast-flying aircraft.” *Atmospheric Measurement Technology*, 9, 5135–5162.

393 Wilson, J. C. and Jonsson, H. (2011). “Measurement of cloud and aerosol particles from aircraft.”  
394 *Aerosol Measurement: Principles, Techniques, and Applications*, P. Kulkarni, P. A. Baron, and  
395 K. Willeke, eds., John Wiley & Sons, 3rd edition, 655–665.

396 Wu, W. and McFarquhar, G. (2016). “On the impacts of different definitions of maximum dimension  
397 for nonspherical particles recorded by 2D imaging probes.” *Journal of Atmospheric and Oceanic*  
398 *Technology*, 33, 1057–1072.



399 **List of Tables**

400 1 Key dimensions of the aircraft. . . . . 18

401 2 CFD model test conditions based on typical scientific flight conditions. . . . . 19

Aircraft Section	Size
Total Aircraft Length (m)	14.31
Wing Span (m)	15.83
Wing Tip Chord (m)	0.83
Tail Span (m)	6.61
Tail Tip Chord (m)	0.65
Fin Tip Chord (m)	0.84
Wing Gross Area (m <sup>2</sup> )	25.60
Aspect Ratio	9.79

**TABLE 1.** Key dimensions of the aircraft.

Parameter	Value
Angle of Attack*, $\alpha$ ( $^{\circ}$ )	3.5 - 6
Slideslip Angle, $\beta$ ( $^{\circ}$ )	-5 - 5
True Airspeed, TAS (m/s)	142.17 - 171.92
Mach Number, M	0.46 - 0.56
Reynolds Number, Re	$1.51 \times 10^7$ - $1.82 \times 10^7$
Altitude (ft)	25,000
Air Density ( $\text{kg/m}^3$ )	0.55
Temperature ( $^{\circ}\text{C}$ )	239
Pressure (Pa)	37600
*AOA= $17.3-0.08(\text{TAS})$	over 3.5-5.5 $^{\circ}$ range

**TABLE 2.** CFD model test conditions based on typical scientific flight conditions.

402  
403  
404  
405  
406  
407  
408  
409  
410  
411  
412  
413  
414  
415  
416  
417  
418  
419  
420  
421  
422  
423  
424  
425  
426  
427

## List of Figures

1	Port side underwing instrument canisters on the aircraft. . . . .	22
2	Plot line for the flow angle and velocity magnitude comparisons for viscous/inviscid analysis in Fig. 4, and the engine operative/inoperative analysis in Fig. 3 . . . . .	23
3	Comparison of flow angles upstream of the canister dome for engine operative and inoperative cases ( $AOA=5^\circ$ , $AOSS=0^\circ$ ). The x-axis is normalised with respect to the length of the plot line, Fig. 2. . . . .	24
4	Comparison of the flow angles upstream of the canister dome for inviscid and viscous solutions ( $AOA=5^\circ$ , $AOSS=0^\circ$ ). The x-axis is normalised with respect to the length of the plot line, Fig. 2. . . . .	25
5	Comparison of flight test and CFD (at comparable flight conditions) predicted AOA (x-z plane) flow angles with reference line correction (Flight test data filtered to include only points with $\pm 0.2^\circ$ AOSS) and 95% confidence intervals applied. . . .	26
6	Pressure contours (x-y plane upper, x-z plane lower) showing areas of high pressure below the wing, behind the engine casing, and on the canister domes, in relation to the AIMMS Probe measurement location. . . . .	27
7	Flow perturbation as a function of TAS in the (a) longitudinal and (b) horizontal from the free-stream conditions as a function of aircraft AOA. Results are shown for each of the four canister positions on each under-wing pylon but do not include the effect of the canisters themselves. . . . .	28
8	The source simulated spherical droplet with digitized CIP images for both the unperturbed airflow case and the case when there is a -20% change in the longitudinal and a 10% change in the transverse airflows. These changes are large but used so that the effect on the particle image is more obvious. . . . .	29
9	Simulated hexagonal plate and associated CIP images. Marked are common measures of particle size, see the text for details. . . . .	30

428 10 Effect on the reported size of a spherical droplet for (a) longitudinal flow velocity  
429 perturbations and (b) transverse flow velocity perturbations from the free-stream  
430 conditions. The sizing definitions are described in the text. The effect of the  
431 transverse velocity, presented as a fraction of the TAS, is small so that there is  
432 significant noise associated with digitization. . . . . 31

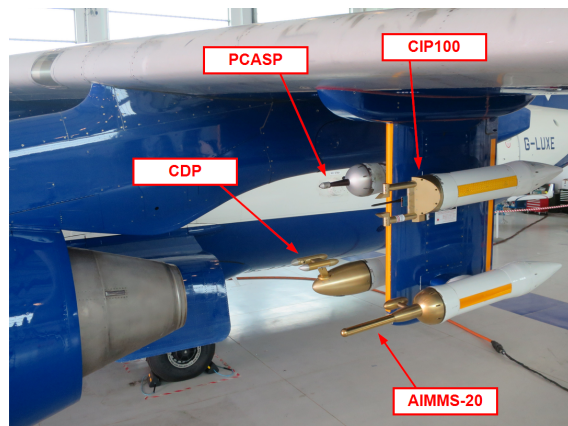
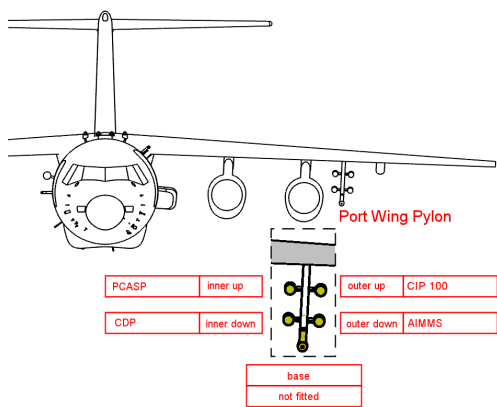


**Fig. 1.** Port side underwing instrument canisters on the aircraft.

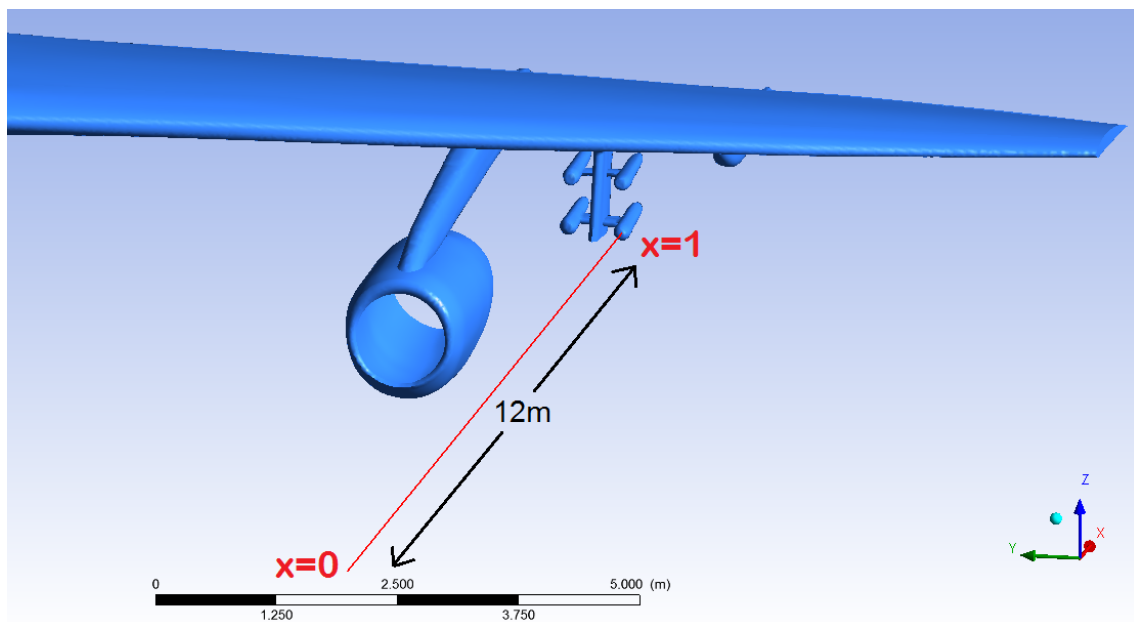


**Fig. 2.** Plot line for the flow angle and velocity magnitude comparisons for viscous/inviscid analysis in Fig. 4, and the engine operative/inoperative analysis in Fig. 3

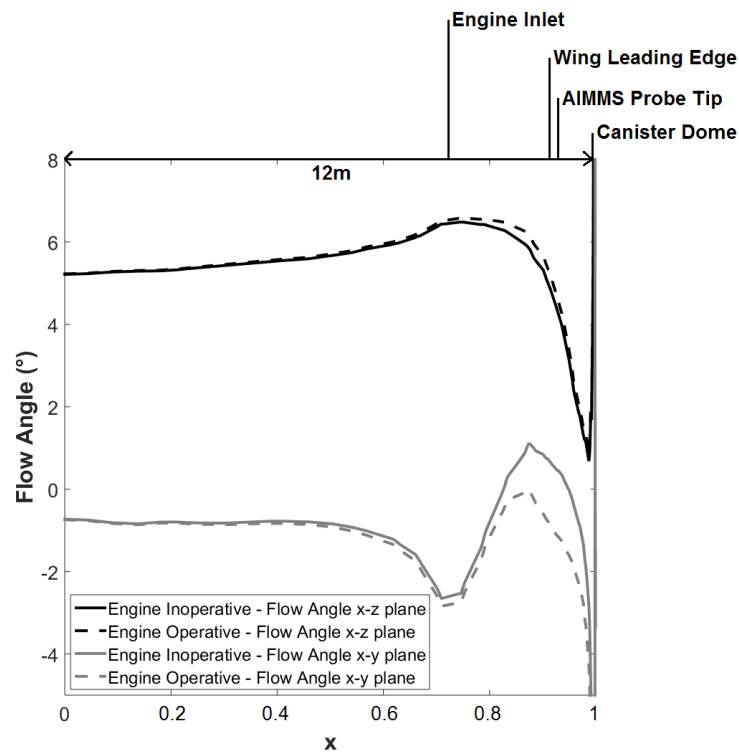


**Fig. 3.** Comparison of flow angles upstream of the canister dome for engine operative and inoperative cases ( $AOA=5^\circ$ ,  $AOSS=0^\circ$ ). The x-axis is normalised with respect to the length of the plot line, Fig. 2.



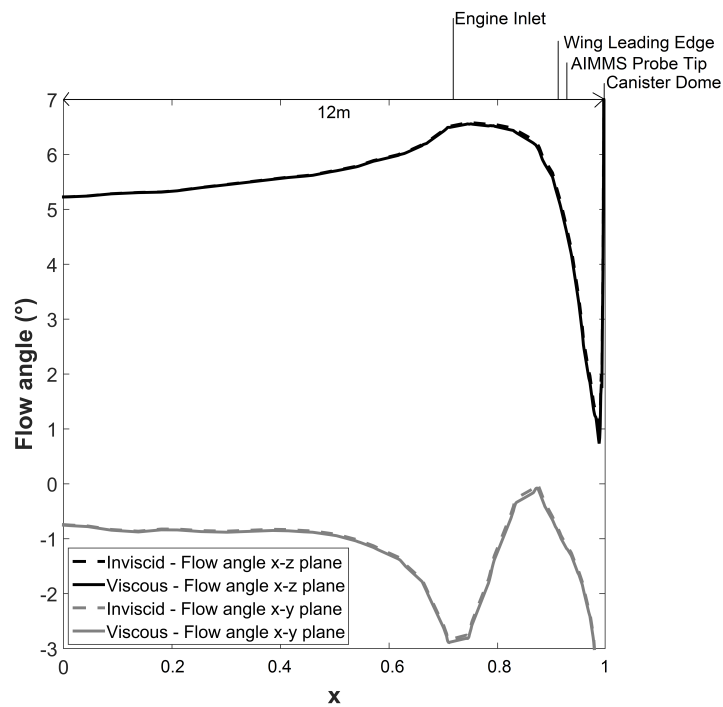


**Fig. 4.** Comparison of the flow angles upstream of the canister dome for inviscid and viscous solutions (AOA=5°, AOSS=0°). The x-axis is normalised with respect to the length of the plot line, Fig. 2.

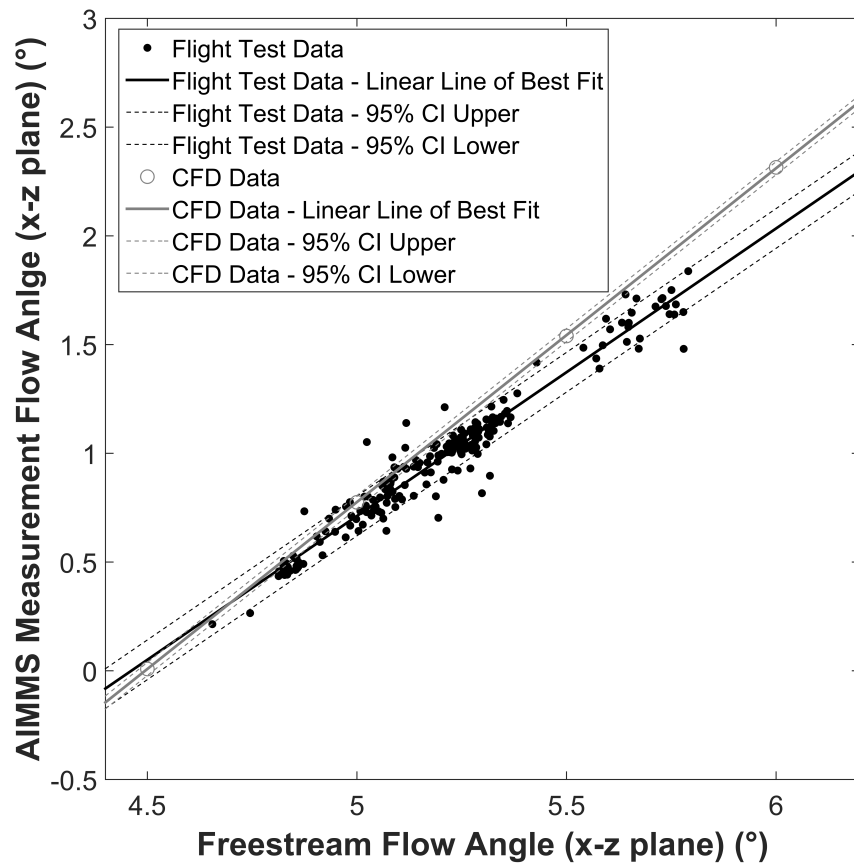


**Fig. 5.** Comparison of flight test and CFD (at comparable flight conditions) predicted AOA (x-z plane) flow angles with reference line correction (Flight test data filtered to include only points with  $\pm 0.2^\circ$  AOSS) and 95% confidence intervals applied.

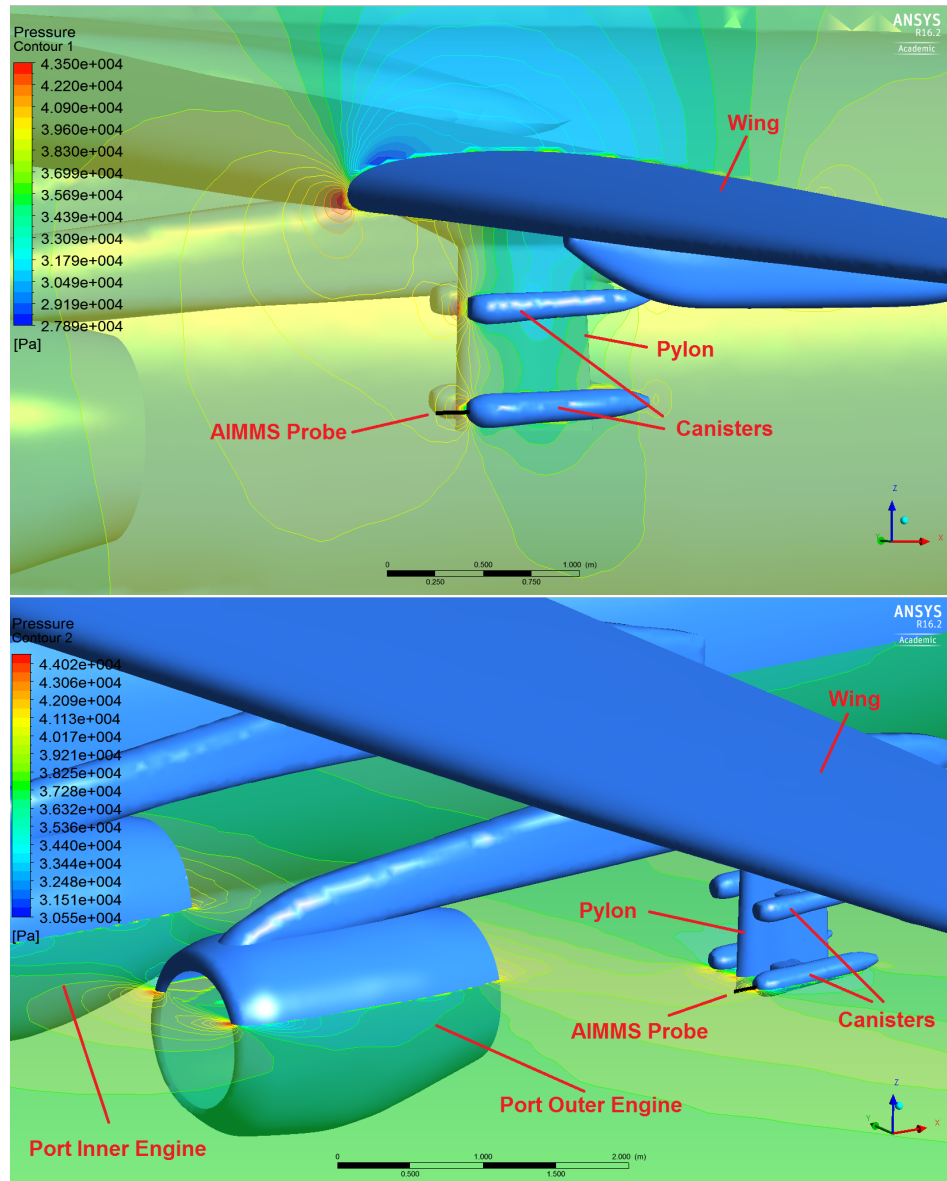


**Fig. 6.** Pressure contours (x-y plane upper, x-z plane lower) showing areas of high pressure below the wing, behind the engine casing, and on the canister domes, in relation to the AIMMS Probe measurement location.

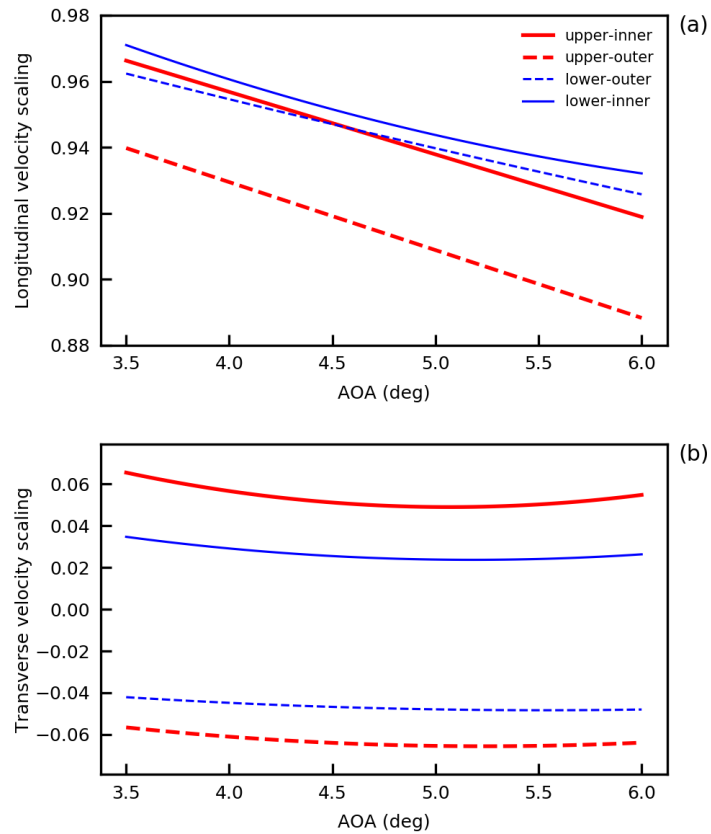


**Fig. 7.** Flow perturbation as a function of TAS in the (a) longitudinal and (b) horizontal from the free-stream conditions as a function of aircraft AOA. Results are shown for each of the four canister positions on each under-wing pylon but do not include the effect of the canisters themselves.

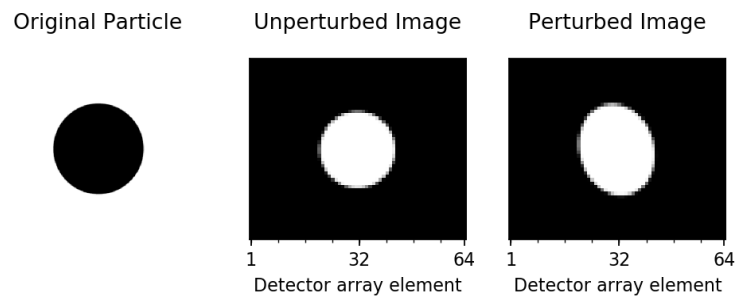


**Fig. 8.** The source simulated spherical droplet with digitized CIP images for both the unperturbed airflow case and the case when there is a -20% change in the longitudinal and a 10% change in the transverse airflows. These changes are large but used so that the effect on the particle image is more obvious.

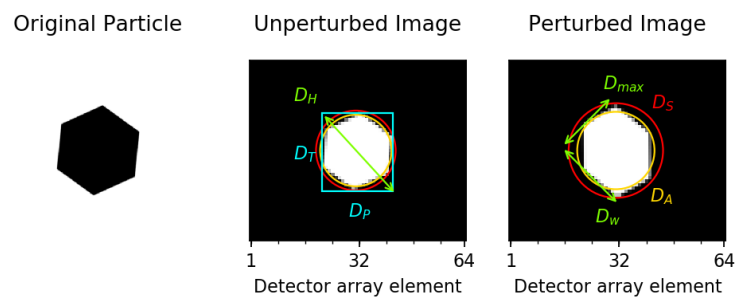


**Fig. 9.** Simulated hexagonal plate and associated CIP images. Marked are common measures of particle size, see the text for details.

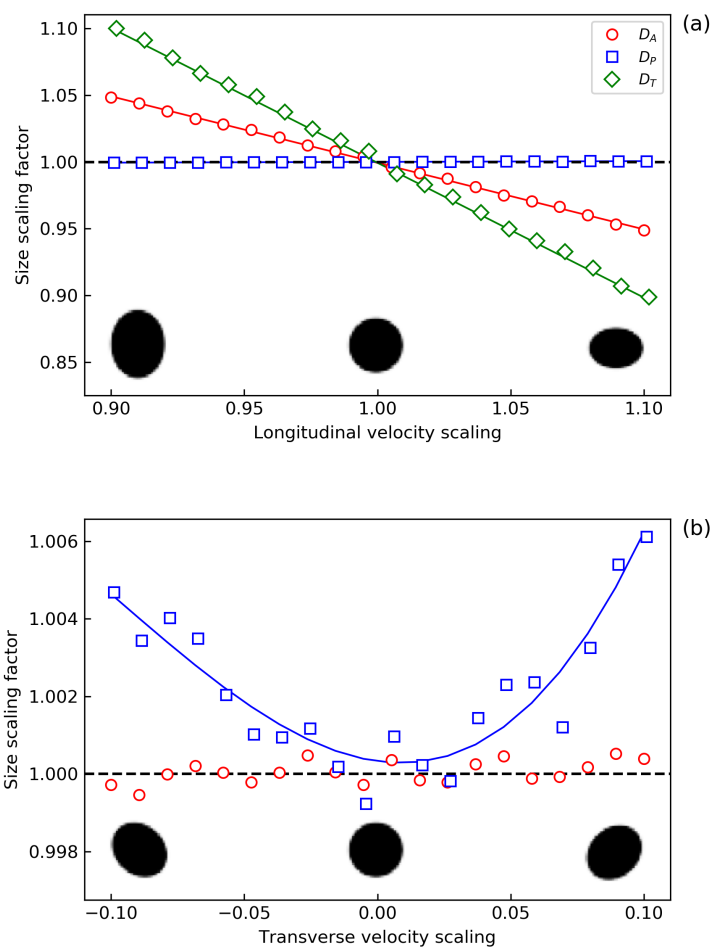


**Fig. 10.** Effect on the reported size of a spherical droplet for (a) longitudinal flow velocity perturbations and (b) transverse flow velocity perturbations from the free-stream conditions. The sizing definitions are described in the text. The effect of the transverse velocity, presented as a fraction of the TAS, is small so that there is significant noise associated with digitization.

# Characterizing instrumentation canister aerodynamics on the FAAM BAe-146-301 atmospheric research aircraft

Bennett, Christopher J.

2019-04-30

Attribution-NonCommercial 4.0 International

---

Bennett CJ, Nott GJ, Wellpott A, Lawson N, Delise M, Woodcock B and Gratton GB.

Characterising instrumentation canister aerodynamics on the FAAM BAe-146-301 atmospheric research aircraft. *Journal of Aerospace Engineering*, Volume 32, Issue 4, 2019

[https://doi.org/10.1061/\(ASCE\)AS.1943-5525.0001044](https://doi.org/10.1061/(ASCE)AS.1943-5525.0001044)

*Downloaded from CERES Research Repository, Cranfield University*